JOURNAL OF SOLID STATE CHEMISTRY **138,** 98–110 (1998)
ARTICLE NO. SC987758

Two-Phase Microstructures Generating Efficient Pinning Centers in the Heavily Pb-Substituted $Bi_2Sr_2CaCu_2O_{8+\delta}$ Single Crystals

Z. Hiroi, I. Chong, and M. Takano

Institute for Chemical Research, Kyoto University, Uji, Kyoto 611-0011, Japan

Received September 15, 1997; in revised form January 5, 1998; accepted January 13, 1998

$Bi_2Sr_2CaCu_2O_{8+\delta}$ (Bi-2212) single crystals with a large amount of Pb substituted for Bi were grown by the floating zone method, and their magnetic properties and microstructures have been studied by means of SQUID magnetometery and electron microscopy. Critical current density (J_c) increases dramatically beyond a critical Pb content of ~ 0.4 per formula unit, where characteristic two-phase microstructures are revealed by electron microscopy. The "single" crystals consist of alternating thin (several tens of nanometers) lamellar plates of two phases with the (010) interface, one with lower Pb content (~ 0.4) and a modulated structure and the other with higher Pb content (~ 0.6) and a modulation-free structure. The relative volume fraction of the latter phase increases systematically with increasing starting Pb content. At higher Pb content, lamellas with irregularly stepped interfaces and bubbles of the latter phase embedded in the matrix of the former phase are also observed. The growth mechanism is discussed in terms of unidirectional solidification of eutectic or eutectoid. © 1998 Academic Press

INTRODUCTION

Among many high-T_c superconductors (HTSCs) studied to date, Bi-2212 has been considered one of the most promising materials for use as wires for cables and magnets because of its chemical stability and morphological properties suitable for manufacturing processing. However, one serious problem which has prevented a large-scale application of this compound is that above 20 K, J_c decreases very quickly with increasing magnetic field. This decrease arises from the breakdown of the zero-resistive state due to thermally activated flux flow, which tends to be accelerated for this compound known for its inherent exceeding two-dimensional anisotropy. Irreversibility line (IL) is a practically important boundary in the H–T phase diagram which marks the boundary between the regions of reversible and irreversible magnetic behaviors (1). It is thought that the vortices are more or less pinned by defects in crystals below the IL, whereas they can move in response to minimal external forces and also thermally above the IL where J_c vanishes. From the viewpoint of applications it is particularly important to expand this irreversible regime and, thereby, increase the practical J_c.

A key to increasing J_c is to generate efficient pinning centers in the crystals. Two types of pinning centers have been known in HTSCs; point disorders (e.g., neutron or electron irradiation-induced defects, impurities, or oxygen vacancies) and correlated defects (e.g., twin boundaries or columnar defects generated by heavy ion irradiation). The former is effective at low temperature, while the latter plays a crucial role at high temperature. Recent studies using heavy-ion irradiation have demonstrated that aligned columnar defects serve as efficient flux pinning centers so that the IL shifts upward (2–8). However, this method is rather inaccessible. We believe that an alternative method of generating efficient pinning centers in a more practical and useful way is necessary for future large-scale applications.

It is well known that Pb can partially replace Bi in the family of Bi superconductors. Pb substitution of about 0.3 per formula unit is essential to the formation itself of $Bi_2Sr_2Ca_2Cu_3O_{10+\delta}$ (Bi-2223) (9), while a range of solid solutions exist for Bi-2212 and $Bi_2Sr_2CuO_{6+\delta}$ (Bi-2201) (10–12). In the case of Bi-2212, a series of single-phase polycrystalline materials were obtained for $0 \le y \le 0.8$ in a formula $Bi_{2-y}Pb_ySr_2CaCu_2O_{8+\delta}$ (10, 13, 14). A small improvement in J_c was reported for the polycrystalline material with $y = 0.4$ (15). Many single-crystal growth experiments have also been carried out, and their properties have been studied (16, 17). Noteworthy here is that a significant enhancement of J_c was reported for a crystal prepared from a melt with a high Pb content of $y = 0.7$ (18, 19).

Recently, we succeeded in growing a series of single crystals of Bi-2212 with various amounts of Pb by the floating zone method and found that the magnetic properties were dramatically improved beyond a critical Pb content (20). The crystals with nominal Pb contents of 0.6 and 0.7 per formula unit exhibited large J_c values, particularly above 30 K, compared with Pb-free crystals. By electron microscopy, moreover, characteristic two-phase microstructures were revealed that probably underlay the observed increase

0022-4596/98 $25.00

in J_c. It was suggested that the interface of the two phases that was always perpendicular to the CuO_2 planes suppressed the thermally activated flux flow and thus worked as efficient pinning centers. A more detailed systematic study of the magnetic properties and the microstructures as a function of Pb content is presented in this report.

EXPERIMENTAL

Single crystals were grown from starting compositions of $Bi_{2.2-x}Pb_xSr_{1.8}CaCu_2O_{8+\delta}$ ($x = 0$, 0.2, 0.4, 0.6, 0.7, 0.8) by the conventional floating zone (FZ) method using an infrared furnace. The starting polycrystalline materials were prepared by the standard solid-state reaction method from Bi_2O_3, PbO, $SrCO_3$, and CuO. After several heat treatments at 720–820°C in air cylindrical rods of 6 mm in diameter and 60 mm in length were made by cold pressing and subsesquent sintering at 840°C for 24 h in air. Then, the rods were mounted in the FZ furnace and densified by moving the molten zone with a high speed of 50 mm/h. For crystal growth, a narrow liquid zone was formed between a pair of rods. The upper and lower rods were counter rotated at 30 rpm, and these were slowly moved downward together at a rate of 0.5 mm/h so that a crystal grew unidirectionally in a temperature gradient along the rods. All the crystals were grown in an atmosphere of 20% O_2/80% N_2. Experiments either in pure O_2 or N_2 were unsuccessful, because the molten zone could not be kept stable. The grown boules consisted of thin rectangular plates elongated along the growth direction, which was parallel to the *a* axis as determined by the Laue method. Single crystals of a few millimeters in edge and less than 0.1 millimeters thick were cleaved from the boules.

A significant evaporation of elements from the melt was noticed during the growth, particularly for high Pb contents. The quality of the $x = 0.8$ crystal was apparently poor. The actual Pb content was examined using energy-dispersive X ray (EDX) analysis in an analytical electron microscope (JEM-2010). The results indicated that about 20 and 30% of Pb was lost for crystals with $x = 0.4$ and 0.6, respectively. Post-annealing at 816°C in air was done for crystals with $x = 0.7$ to investigate the stability of the microstructures found in the as-grown crystals.

Magnetization measurements were carried out for as-grown crystals in a SQUID magnetometer (MPMS-XL, Quantum Design) with a 2-cm scan length with *H* approximately parallel to the *c* axis. Single crystals of a typical size of $1.0 \times 1.0 \times 0.03 \sim 0.05\ mm^3$ were used.

High-resolution electron microscopy (HREM) observations were carried out in a transmission electron microscope (JEOL-2000EX) operated at 200 kV. We prepared specimens for observation in two ways. One method for a "plan-view" observation was crushing, dispersing in acetone, and collecting on a holey carbon film supported by a copper grid. The other method for a "cross-sectional" observation was direct thinning using an ultramicrotome (LKB-2188) with a diamond blade. First, a few tens of μm thick crystal was embedded in epoxy resin. After curing at 60°C for 24 h, slices less than 50 nm thick were cut from this block with the diamond edge. The cutting direction was chosen perpendicular to the crystal plate. Then, the slices were mounted on a microgrid and examined by the electron microscope.

MAGNETIC PROPERTIES

Magnetization measurements were carried out with *H* approximately parallel to the *c* axis of each crystal. Figure 1 compares the temperature dependence of magnetization for four crystals ($x = 0.0$, 0.4, 0.6, 0.7) in an applied field of 1 kOe. The T_c onset varied slightly with Pb content as 87, 85, 83, and 85 K for $x = 0$, 0.4, 0.6, and 0.7, respectively. It was reported in a previous study on polycrystalline samples annealed at 750°C in nitrogen flow that T_c was raised above 90 K by the Pb substitution (10). The observed decrease in T_c for the present crystals prepared in air must be due to the overdoping effect resulting from higher oxygen content. In fact, the T_c was found to increase from 83 to 96 K for our $x = 0.6$ crystal after annealing at 700°C in $P_{O_2} = 3.5 \times 10^{-4}$ atm (21).

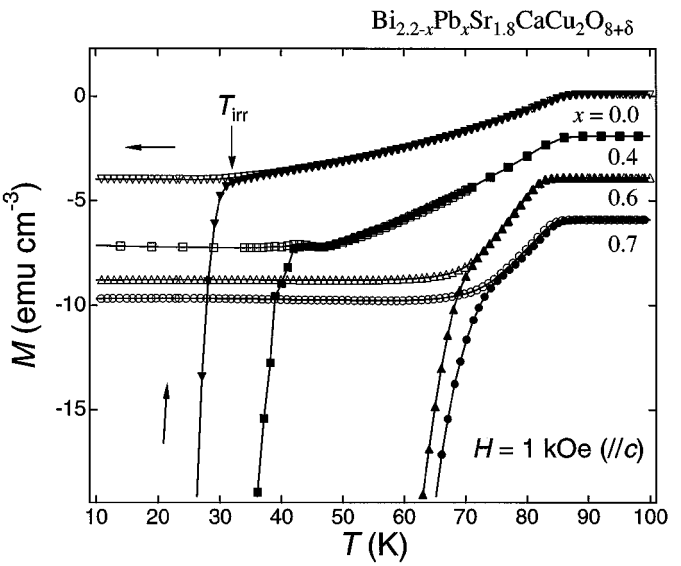

FIG. 1. Comparison of the temperature (T) dependence of magnetization (M) for the pure ($x = 0$) and the Pb-doped ($x = 0.4$, 0.6, and 0.7) single crystals. The data for $x = 0.4$, 0.6, and 0.7 are shifted downward by 2, 4, and 6 emu/cm^3, respectively, for clarity. The measurements were carried out in a SQUID magnetometer with a 2-cm scan length with *H* approximately parallel to the *c* axis. In each measurement, the sample was rapidly cooled down to 10 K in nearly zero field, warmed slowly up to 100 K in an applied field of 1 kOe (ZFC, solid symbols), and cooled again down to 10 K (FC, open symbols).

A large hysteresis was observed for each crystal below the irreversible temperature, T_{irr}, where the zero-field-cooled (ZFC) and the field-cooled (FC) branches separated. In the reversible region, vortices cannot be pinned by defects in crystals, and, thus, J_c becomes nearly zero owing to thermally activated flux flow. For pure Bi-2212, T_{irr} was much lower than T_c, whereas Fig. 1 shows that T_{irr} was dramatically increased with increasing Pb content; 32, 43, 70, and 75 K for $x = 0.0, 0.4, 0.6$, and 0.7, respectively. The T_{irr} for $x = 0.8$ was nearly equal to that for $x = 0.7$. This result suggests that the Pb substitution suppresses flux flow and leads to an increase in J_c at high temperature as for ion-irradiated crystals with columnar defects (2–8).

The ILs for the crystals in our study were determined by magnetization measurements as a function of temperature and field as shown in Fig. 2. The IL shifted markedly upward with Pb substitution, especially for $x = 0.6$ and 0.7. The H_{irr}'s of the $x = 0.6$ and 0.7 crystals are slightly smaller than those reported for heavy-ion irradiated single crystals below 40 K (8) but significantly larger at higher temperatures.

We estimated the temperature dependence of J_c through magnetic measurements at fixed temperatures using the Bean model (22); in this model the hysteresis in magnetization, ΔM [emu/cm^3], is related to J_c [A/cm^2] as $J_c = 20\Delta M/r$, where r [cm] is the radius of the circulating current which was assumed to be the lateral dimension for the present crystals. Figure 3 presents the results for $x = 0.0$, 0.4, 0.6, and 0.7 at $H = 1$ kOe applied along the c axis. The absolute value for the pure crystal was nearly equal to those reported previously (4), whereas the values for the $x = 0.6$ and 0.7 crystals at 20 K were larger by one order of magnitude. J_c fell rapidly with increasing temperature for $x = 0$ and 0.4, but the Pb substitution up to $x = 0.7$ suppressed the drop, maintaining J_c well above 10^4 A/cm^2 up to $T = 60$ K. These results demonstrate that very efficient pinning centers, which must be associated with the heavy-Pb substitution, were introduced into the present crystals.

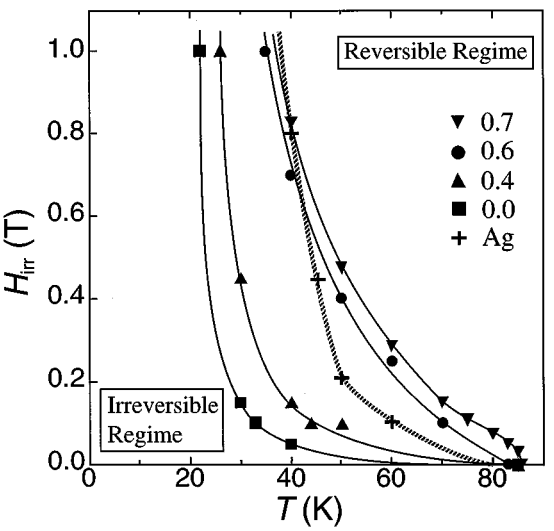

FIG. 2. Plots of the irreversibility field (H_{irr}) as a function of temperature for $x = 0$, 0.4, 0.6, and 0.7. The data points were determined by the measurements of M–T or M–H curves. The solid lines are guides to the eye. Also plotted for comparison is the H_{irr} of a Bi-2212 single crystal irradiated with 200-MeV Ag ions (8). Note that the H_{irr} at $T > 40$ K is significantly larger in the pressent Pb-doped crystal ($x = 0.6$ and 0.7) than in the heavy-ion irradiated one.

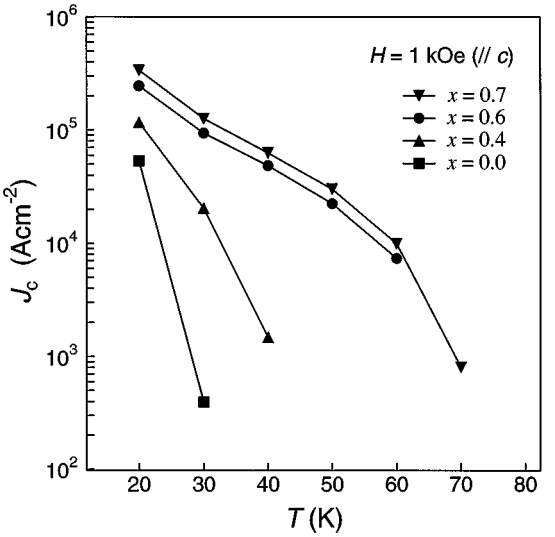

FIG. 3. Comparison of the temperature dependence of J_c for the four crystals at $H = 1$ kOe. The J_c's were determined using the Bean model from M–H hysteresis loops measured in a SQUID magnetometer.

Wang *et al.* reported J_c values of $\sim 10^6$ and 5×10^3 A/cm^2 at 10 and 30 K, respectively, in an applied field of 4 kOe for their $Pb_{0.7}Bi_{1.4}Sr_{1.6}Ca_{0.7}Cu_{1.8}O_z$ crystal (18). To be compared with these values are $\sim 10^6$ and 7×10^4 A/cm^2 obtained under the same conditions for the $x = 0.7$ crystal in our study. It is apparent from this comparison that our crystals show much higher J_c than Wang's crystal at elevated temperatures. This difference in J_c at high temperatures must reflect an essential difference in the inherent pinning mechanism between their and our crystals. They suggested that the increase of J_c was attributable to disordering of the modulation, though the relevance was not clear from their experiments dealing with only one Pb composition. The difference in the pinning mechanism between their and our crystals must arise from the difference in actual Pb content in crystals or in the microstructures determined by the crystal-growth method; their crystal was grown from CuO-rich melts by slow cooling.

STRUCTURAL PROPERTIES

Modulated Structure

Bi compounds exhibit a unique one-dimensionally modulated structure along the b axis in which atomic positions are displaced in a wavy manner (23–26). The wavelength along the b axis is $4.8b$ ($b \sim 0.54$ nm), but increases monotonically with Pb substitution; wavelengths of $6.0b$ to $7.3b$ were reported for $y = 0.2$ to 0.3 in $Bi_{2-y}Pb_ySr_2CaCu_2O_{8+\delta}$ (10, 27–29) and also of $8.2b$ to $9.2b$ for $y \sim 0.4$ (30). Even the disappearance of the modulation was reported for $y \geq 0.6$ (10, 13) or for $y \geq 0.48$ (30) in polycrystalline samples. Thus, the modulation wavelength can be an approximate measure of the actual Pb content in crystals.

Electron diffraction (ED) experiments were done to determine the modulation wavelength, λ. About 10 fragments obtained by crushing a piece of crystal were examined for each composition. A typical ED pattern is reproduced in Fig. 4. It was recorded from the $x = 0.6$ crystal with an incident electron beam parallel to the $[10\bar{1}]$ direction which was tilted by about 10° from the [001] direction. Rather intense satellite reflections arising from the modulation were excited for this zone axis, as compared with those in the [001] zone. The λ was determined from the spacings between a fundamental spot and the corresponding first-order satellite spots. Its composition dependence is shown in Fig. 5. λ increases initially with increasing Pb content, but saturates for $x \geq 0.6$ where two phases coexist. However, one must take into account considerable loss of Pb during the crystal growth to interpret this composition dependence. In order to determine the composition dependence of λ in a more reliable way, ED experiments were carried out also on a series of polycrystalline samples which were prepared from the same starting compositions at 820°C in air without a melting process and finally annealed at 740°C in Ar flow. λ measured for the polycrystalline samples increased more rapidly with x, and reached $10–12b$ at $x = 0.5$. Then, the superstructure disappeared completely for $x = 0.6$ as previously reported for the $Bi_{2-y}Pb_ySr_2CaCu_2O_{8+\delta}$ series with $y = 0.6$. The difference between the two curves in Fig. 5 may suggest that the loss of Pb is relatively small in the polycrystalline samples compared to the single crystals.

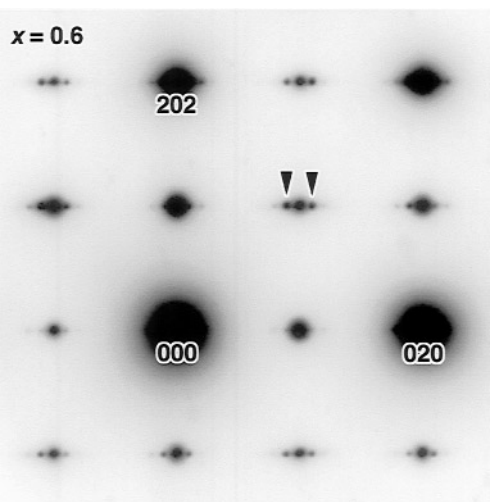

FIG. 4. Electron diffraction pattern of the $x = 0.6$ crystal taken with the incident electron beam parallel to the $[10\bar{1}]$ direction. Satellite reflections arising from the structural modulation appear on both sides of the fundamental spots along the b^* axis as typically marked with the arrows near the (111) reflection. From the spacing of the spots, the modulation wavelength was determined to be 5.24 nm ($9.7b$). The HREM image corresponding to the ED pattern is shown in Fig. 7.

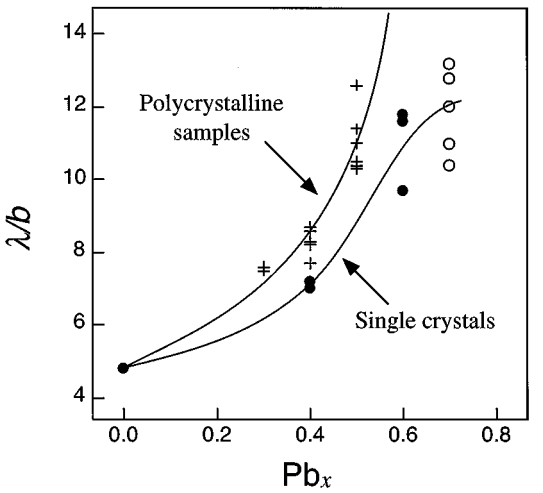

FIG. 5. Composition dependences of the modulation wavelength (λ) for a series of single crystals (circle) and for a series of polycrystalline samples (cross). The data for the $x = 0.6$ and 0.7 crystals were obtained from α-phase domains. The λ for the polycrystalline series seemed to diverge toward infinity at $x = 0.6$, where the modulation was absent.

Plan-View HREM Observations

We examined the evolution of microstructures with Pb content for the crystals with $x = 0.4$, 0.6, 0.7, and 0.8 by plan-view HREM observations. Several to 10 thin fragments obtained by crushing were examined for each crystal. The incident electron beam was always chosen to be parallel to the $[10\bar{1}]$ direction so that the b axis was perpendicular to the incident beam. The satellite reflections arising from the modulation were strongly excited in this zone axis, and, thus, the corresponding long-period lattice fringes were clearly visible in the HREM images.

$x = 0.4$ crystal. Almost all the thin Fragments, except 1 out of 10, of the $x = 0.4$ crystal exhibited featureless images in low magnifications as typically shown in Fig. 6a. Under magnification, however, very regular long-period fringes corresponding to the modulation with $\lambda = 3.9$ nm

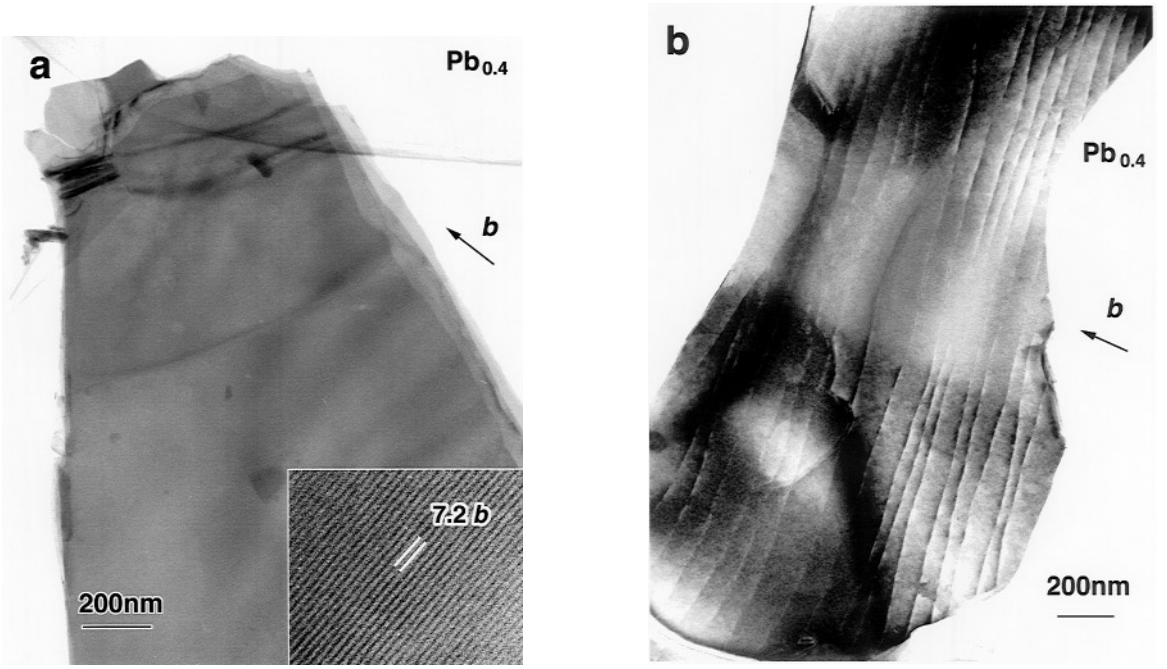

FIG. 6. Typical high-resolution electron microscopy image for $x = 0.4$, showing (a) a homogeneous morphology and (b) an exceptional image with curved strings. The incident electron beam was parallel to the $[10\bar{1}]$ direction so that the b axis was perpendicular to the incident beam. In (a) long-period fringes with a spacing of $7.2b$ (see an enlargement in inset) arising from the modulation are extended over the entire particle. Similar fringes are also seen in the areas between the strings in (b).

($7.2b$) were apparent along the b axis over the entire particle, which suggested that Pb was uniformly incorporated into the crystal. The HREM image of the one exceptional fragment is shown in Fig. 6b. The normal, regular modulation wave with $\lambda = 7.0b$ was seen, but, in addition, slightly curved strings with a strong diffraction contrast appeared with spacings of 50–150 nm along the b axis.

$x = 0.6$ crystal. In distinct contrast to the above observations for $x = 0.4$, all the fragments of $x = 0.6$ exhibited unusual microstructures. Bright horizontal stripes about 10 nm wide were apparent (Fig. 7a). These usually continued from one side of the particle to the other side but sometimes terminated within the particle. The spacing between two adjacent stripes was 50 to 100 nm. Their density varied slightly from fragment to fragment, but the stripes were always present. These domains were thought to have a thin, plate-like shape aligned edge-on, because the diffraction contrast was very strong and the boundary with the matrix was sharp. Under magnification an 8-nm-thick plate-like domain was seen embedded in the matrix (Fig. 7b). Long-period fringes with $\lambda = 9.7b$ arising from the "normal" modulation were visible in the matrix, but such a superstructure was not discernible within the central domain. This finding implies a modulation-free structure or a long periodicity of larger than 8 nm.

We note here that the specific image with strings found in the exceptional fragment for $x = 0.4$ (Fig. 6b) may correspond to the above type of microstructure with extremely thin domains embedded in the matrix.

$x = 0.7$ crystal. As the Pb content increased to 0.7, the microstructure became more pronounced. The volume fraction of the modulation-free lamellas was increased and became comparable with that of the modulated lamellas, giving rise to a striking zebra pattern. Figure 8 shows a typical HREM image for $x = 0.7$. Stripes about 50 nm thick without any modulation wave appear alternately with stripes of a similar thickness where modulation fringes with $\lambda = 11b$ are seen. Note that this feature is quite regular over the entire particle. The periodicity of the alternation along the b axis is about 100 nm, which did not change significantly from fragment to fragment. The interface was always perpendicular to the b axis. Another example is given in Fig. 9, where the two kinds of lamellas are both 30 to 40 nm thick. Modulation waves are definitely absent in every second lamella. A sharp, coherent interface perpendicular to the b axis is also apparent (Fig. 9b). The modulation waves are slightly irregular, compared with those seen for $x = 0.4$. However, the average periodicity is nearly the same, $\sim 11b$, for every lamella, suggesting that the Pb concentration is identical for all the modulated domains. Moreover, the

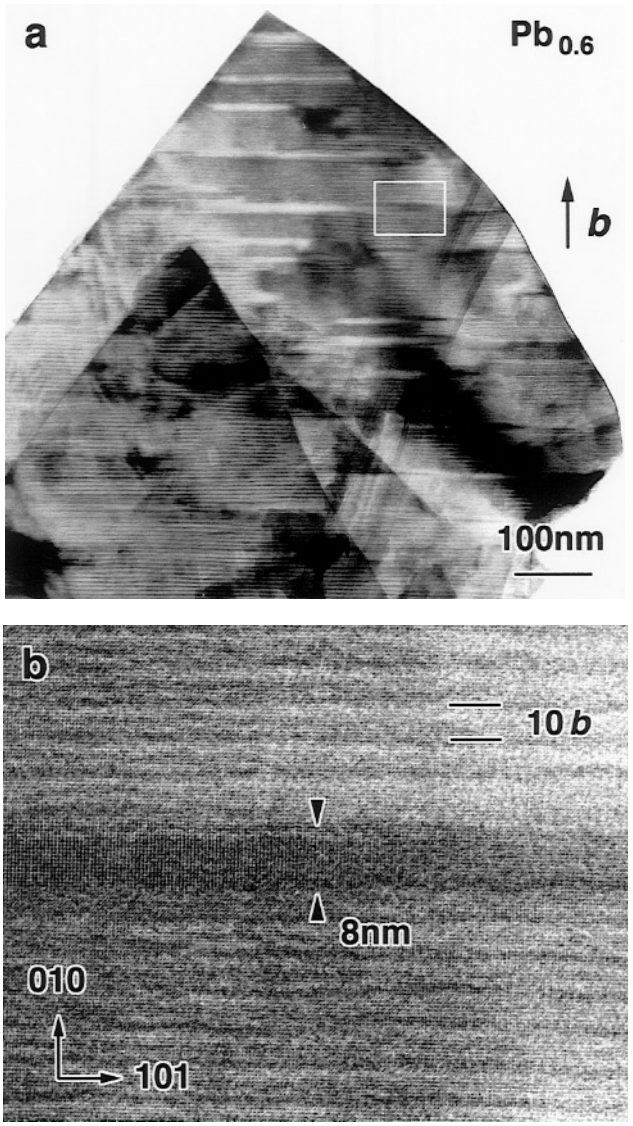

FIG. 7. Electron micrographs showing a typical microstructure for $x = 0.6$. The incident electron beam was parallel to the $[10\bar{1}]$ direction. Horizontal stripes about 10 nm thick appear with a strong diffraction contrast. The wide stripe contrast seen from the right-middle to the center-bottom in (a) is the supporting carbon film. (b) is an enlargent from the rectangle present in (a). The thickness of the stripe is 8 nm. Long-period fringes arising from the modulation with $\lambda = 10b$ (5.4 nm) are seen in the matrix above and below the stripe.

FIG. 8. Typical morphology for $x = 0.7$ taken with the $[10\bar{1}]$ incidence showing a regular zebra pattern.

sharpness of the interface between the alternating domains implies a stepwise change in Pb content without any significant composition gradient. Thus, it is concluded that the crystal consists of alternating thin lamellar plates of two kinds of Pb-substituted Bi-2212 phases. We shall call these phases with and without the structural modulation α and β, respectively.

Most crystals examined possessed the lamella-type two-phase microstructure, but another type of morphology was also found particularly for $x = 0.7$ and 0.8. As typically shown in Fig. 10, it contained bubble- or rod-like modulation-free regions embedded in the modulated matrix phase. The shape of the β domains was almost round, but slightly elongated along the a axis, approximately 100–200 nm along the a axis and approximately 50 nm along the b axis. The distance between adjacent β domains was approximately 50–200 nm. The λ of the α phase deduced from the ED pattern was $13b$, significantly larger than those found in the lamellar structure.

$x = 0.8$ crystal. The $x = 0.8$ crystal was found to be more inhomogeneous with respect to microstructure than for $x \leq 0.7$. Fragments featured by bubble domains were often seen, and sometimes two types of microstructure coexisted. Even in fragments with the lamella-type domains, the interface was often found to be inclined from the (010) plane. Figure 11 presents an image of a fragment showing such rough and inclined interfaces. The volume fraction of the β phase is now larger than that of the α phase. The satellite

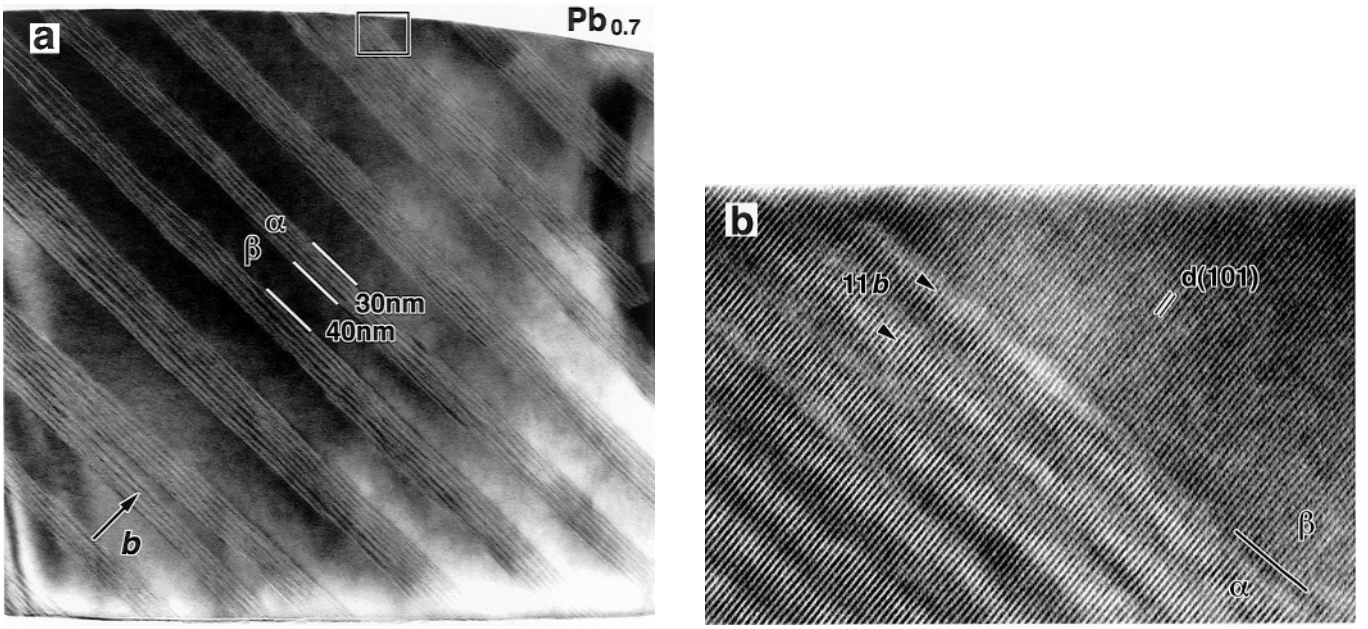

FIG. 9. Electron micrograph of another fragment of $x = 0.7$. The presence of modulation fringes in α domains and their absence in β domains are evident in (a). (b) is an enlargement from the rectangle marked in (a) near the crystal edge. A wavy variation in contrast with $\lambda \sim 11b$ is seen in the α domain. The (101) lattice fringes cross the interface without any discontinuity, indicating a coherent lattice matching without the formation of dislocations.

reflection spots in the corresponding ED pattern were heavily elongated along the b^* axis, reflecting serious disordering in periodicity. A few completely modulation-free fragments were also found for $x = 0.8$.

Cross-Sectional Observations

In order to determine the three-dimensional shape of the two-phase structures, cross-sectional observations were done for the $x = 0.7$ crystal. A rectangular-shaped plate crystal about 30 μm thick was embedded in epoxy resin, and thin slices were cut off to enable HREM observations with electron beam along the a axis. A sliced specimen obtained as above was found to be very uniform in thickness and thin enough for HREM observations, though it was fractured from place to place owing to the damage of mechanical thinning. More microscopic fractures and scratches were also observed.

Figure 12 shows a typical low-magnification image, revealing the good structural coherence of lamellar domains along the c axis. The direction of the electron beam was [10 0 1] that is about 30° tilted from the a axis to the c axis. Vertical stripes a few tens of nanometers thick continued from the top surface of the crystal to the bottom for more than 10 μm, though some discontinuities due to termination or lateral shearing were seen occasionally. The alternation of the two kinds of lamellas was quite regular in the macroscopic scale. The periodicity of $\sim$100 nm coincides with those found in the plan-view observations. Under magnification (Fig. 12b), the thickness of the α and β plates is 60 and 30 nm, respectively, and the interface is sharp parallel to the (010) plane. The modulation waves in the α phase appear considerably disordered. From both the plan-view and the cross-sectional observations, therefore, it is concluded that each domain possesses a thin plate-like shape extending over the entire crystal along the (010) plane.

In minor areas of the same specimen, we found β domains with poor coherence along the c axis (Fig. 13), which may correspond to the bubble domains seen in the plan-view observations (Fig. 10). They also look like mole tunnels or islands approximately 50–80 nm wide along the b axis.

Composition Analysis

We determined the relative abundance of Bi and Pb by means of EDX using focused electron beams (30 nm in diameter) for $x = 0.2$, 0.4, and 0.6. A sharper beam of $\sim$3 nm in diameter was also used to decide the local composition for the $x = 0.7$ crystal in order to probe into the origin of the observed two-phase microstructures. Since these elements have characteristic X rays of similar energies, the absorption correction was assumed to be negligible.

The existence of Pb in crystals was clearly detected by measuring EDX spectra around 10–14 keV, where the Pb Lα and Lβ peaks were seen as shoulders on the low-energy side of the Bi Lα and Lβ peaks, respectively. The Lβ peaks

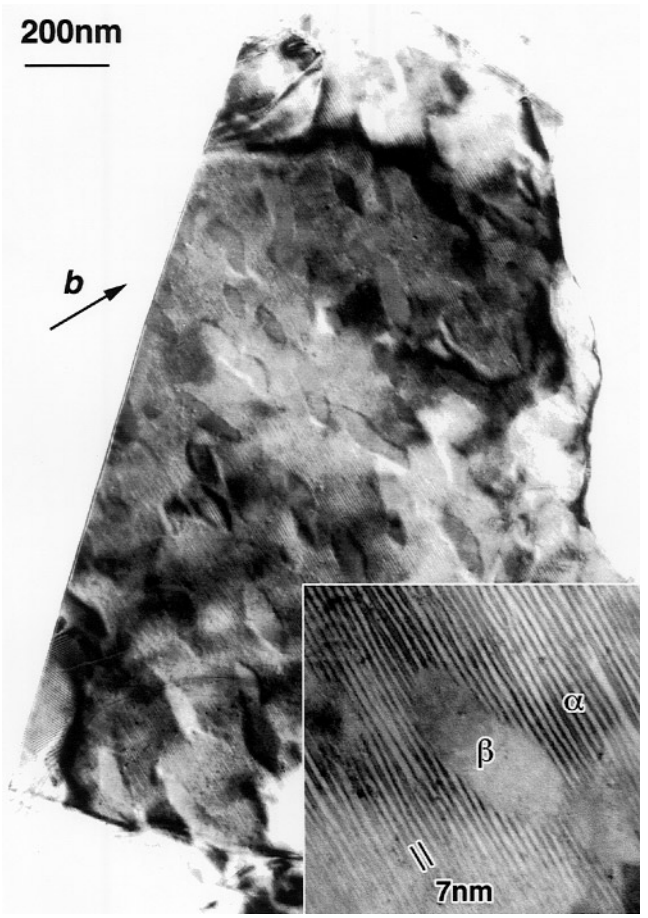

FIG. 10. Electron micrograph showing another morphology found for $x = 0.7$. The modulation-free β domains possess a round shape slightly elongated along the a axis and are embedded in the matrix of the α phase with $\lambda = 7$ nm (13b). The spacing between adjacent β domains is 100–200 nm.

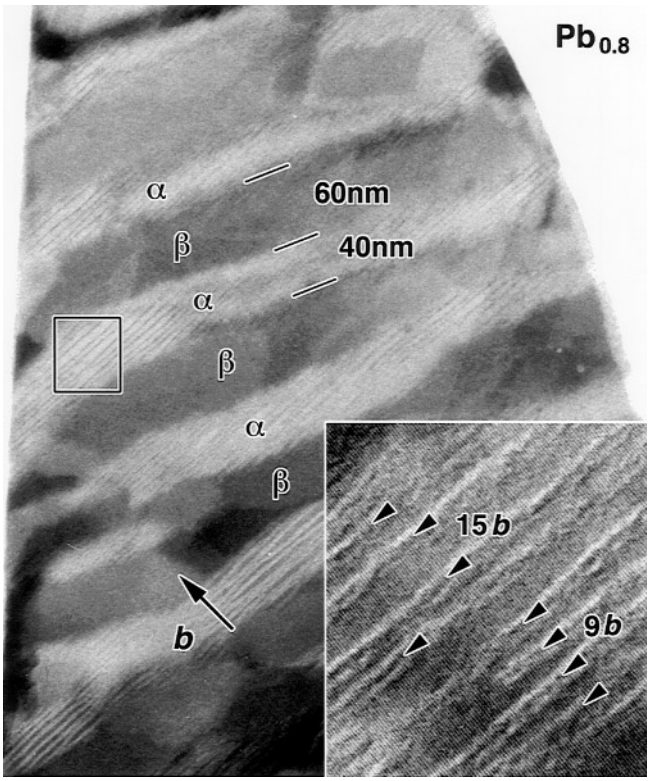

FIG. 11. Irregular lamella structure with rough interfaces inclined from the (010) plane found for $x = 0.8$. The inset is an enlargement from the rectangle marked in the image. The modulation waves are considerably disordered.

were used to evaluate the Pb-to-Bi ratio for its higher resolution. There are four Lβ lines for both the elements; (energy (keV), intensity) = (12.61, 53), (12.62, 20), (12.79, 6), and (12.31, 4) for Pb Lβ_1, Lβ_2, Lβ_3, and Lβ_4, respectively; (13.02, 52), (12.98, 20), (13.21, 6), and (12.69, 4) for Bi Lβ_1, Lβ_2, Lβ_3, and Lβ_4, respectively. The Lβ_1 and Lβ_2 lines lie close to each other for each element and thus appear as a single peak in the present EDX spectra measured with an experimental resolution of 0.155 keV. Therefore, we fitted the data by assuming one intense Gaussian peak involving Lβ_1 and Lβ_2 and two other weak peaks due to Lβ_3 and Lβ_4 with specific intensities fixed as above (Fig. 14). Then, the intensity ratio of the Lβ_1 + Lβ_2 peaks from Pb and Bi was calculated and considered to represent the Pb/Bi molar ratio.

The EDX molar ratio I_{Pb}/I_{Bi} is plotted in Fig. 15, where the data for the $x = 0.6$ crystal was obtained from the modulated α phase region. It is apparent from the figure that a considerable amount of Pb was lost in the crystal growth process, i.e., about 20% and 30% for $x = 0.4$ and 0.6, respectively. The loss seems to increases with increasing Pb content. This loss must be the reason why the modulation wavelength decided for the present series of crystals was smaller than for the polycrystalline series (Fig. 5).

Here, we consider the examination of the two-phase microstructures of the $x = 0.7$ crystal specifically. Two typical fragments examined are shown in Fig. 16; one with regular lamellar domains (a) and the other with bubble domains (b). The approximate positions and the size of the electron probe used are indicated on each image. The effective probe size may be slightly expanded from 3 nm in a crystal, but would be small enough to examine a single domain.

In both types of fragments, a remarkable difference in the relative peak intensity was detected between the α and β domains (Figs. 16c and 16d). The Pb Lβ_1 + Lβ_2 peak was apparently larger for the modulation-free β domains (A, C, P, R) than for the modulated α domains (B, Q). The values averaged over several domains were 0.23 and 0.35 for α and β domains, respectively, which would correspond to $x' = 0.41$ and 0.57 in the formula of $Bi_{2.2-x'}Pb_{x'}Sr_{1.8}$

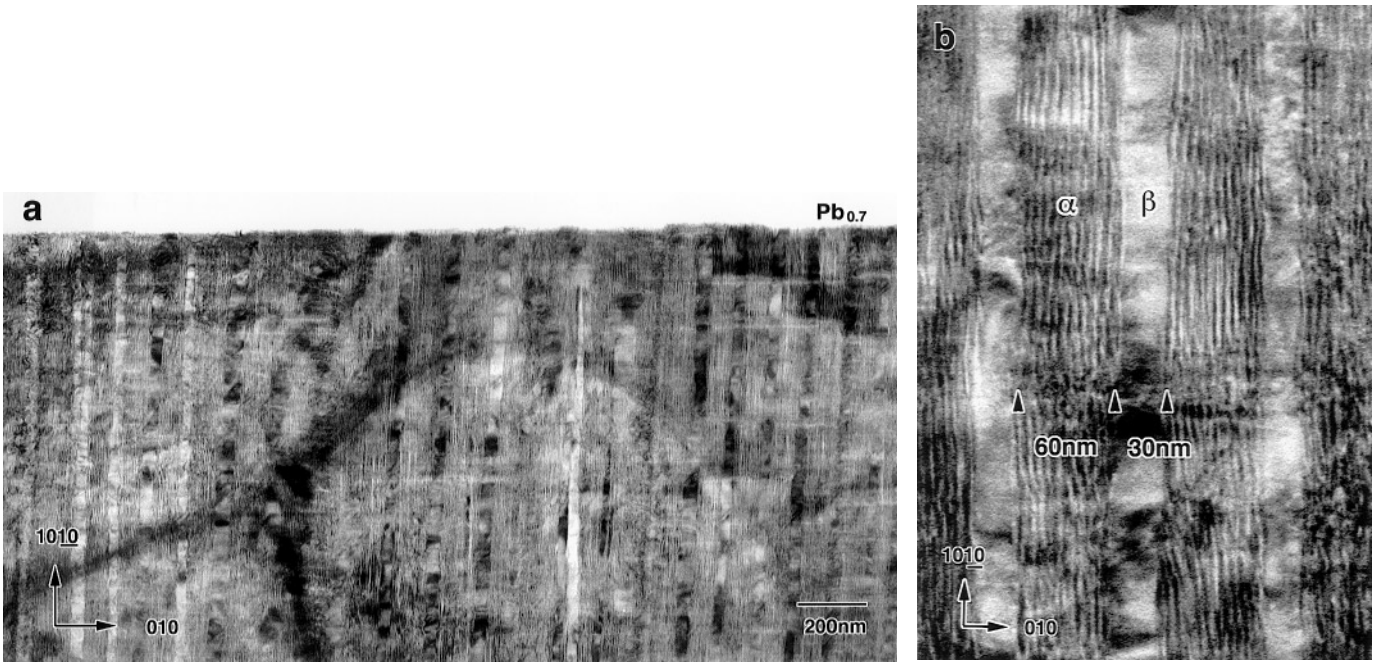

FIG. 12. Electron micrographs showing a "cross-sectional" view of the $x = 0.7$ single crystal. The incident electron beam was parallel to the [10 0 1] direction that was tilted by 30° from [100] toward [001]. The top edge of (a) is the crystal surface. The continuation of each domain along the c axis is apparent. (b) is an enlargement showing a distinct difference in contrast between the two lamellas.

$CaCu_2O_{8+\delta}$. It is important to note that the value of $x' = 0.41$ for the α domains of $x = 0.7$ is nearly equal to that found for $x = 0.6$ (Fig. 15). It means that the practical Pb content of α domains saturates around $x' \sim 0.4$ for starting compositions of $x \geq 0.6$ and, therefore, excess Pb condenses in β domains up to $x' \sim 0.6$. This is in fact consistent with the HREM observations that the relative volume fraction of β domains increases systematically with x. Since the modulation was found to disappear for $x \geq 0.6$ in the polycrystalline samples (Fig. 5), the absence of the modulation in β domains with $x' \sim 0.6$ is quite reasonable. Therefore, we conclude that the entity of the β domain is a Pb-rich, modulation-free crystal, and that the observed two-phase microstructures are associated with the local disproportionation in Pb concentration.

Disappearance of the Two-Phase Microstructures

An annealing experiment was performed on the $x = 0.7$ crystal to investigate the stability of the two-phase microstructures at elevated temperatures. A piece of crystal was cleaved into two thin plates, and one of them was annealed at 816°C in air for 12 h and quenched to room temperature. The metallic luster of the crystal was not lost during this annealing, suggesting that the segregation of Pb compounds like Ca_2PbO_4 did not occur. Both of them were crushed and examined in an electron microscope. It was found, surprisingly, that the two-phase microstructure had completely disappeared after this annealing. This result strongly suggests that the compositional modulation present in the as-grown crystal was wiped out by the annealing, and a uniform solid solution with an intermediate Pb content between $x' \sim 0.4$ and 0.6 was stabilized at high temperature. The two-phase microstructures should have been produced at temperatures lower than 816°C. Further details on the annealing experiments and the resulting change in magnetic properties will be reported elsewhere.

DISCUSSION

Phase Separation

Summarizing the electron microscopy experiments, the heavily Pb-substituted Bi-2212 single crystals exhibited unique two-phase microstructures such as illustrated schematically in Fig. 17. The crystals were uniform with respect to both composition and structure for $x < 0.6$ ($x' < 0.4$), where $x(x')$ is the starting (final) Pb composition in the formula of $Bi_{2.2-x(x')}Pb_{x(x')}Sr_{1.8}CaCu_2O_{8+\delta}$. In contrast, when the total Pb content increased above a critical value around $x = 0.6$, thin lamellar domains with a modulation-free structure and a Pb-rich composition of $x' \sim 0.6$ appeared alternately with modulated, Pb-poor lamellas with $x' \sim 0.4$. The composition of $x' = 0.4$ seems to be the solubility limit of Pb in the modulated domains. The interface

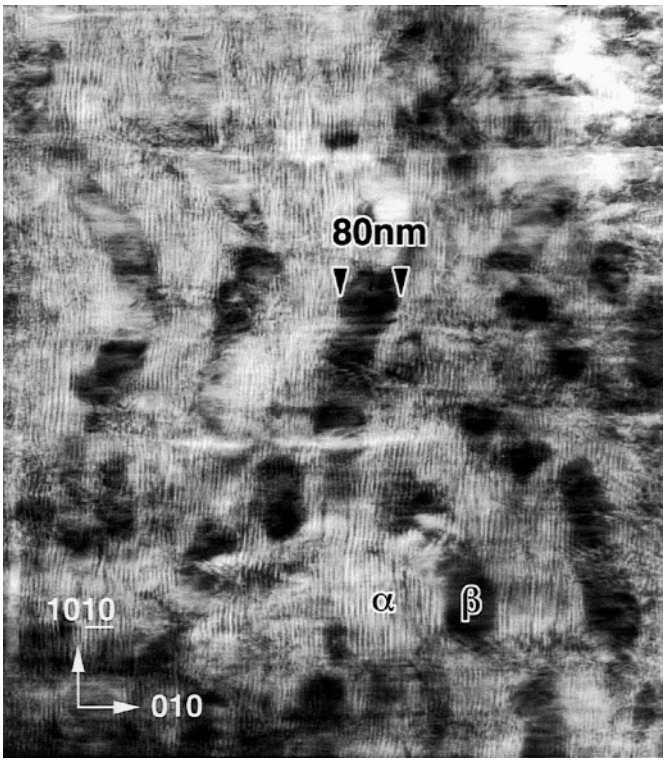

FIG. 13. Cross-ssectional image for $x = 0.7$ illustrating the occurrence of modified structures like mole tunnels or bubbles. On either side of this area there was a much larger region with a regular lamellar structure.

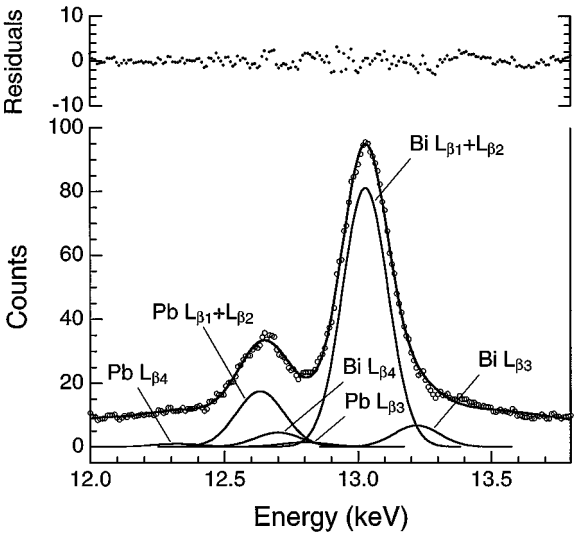

FIG. 14. EDX spectra for $x = 0.6$ in an energy region including the Bi Lβ and Pb Lβ lines. The data (open circles) was taken with an electron probe ~ 30 nm in diameter focused on the area with uniform structural modulations. The calculated components and the sum are shown with the thick lines. The residuals of the fitting are also shown.

was coherent and perpendicular to the b axis of the fundamental lattice. The volume fraction of the Pb-rich phase increased with increasing total Pb content and became nearly half around $x = 0.7$. Further increase in Pb content resulted in irregularities like inclined interfaces and bubbly β domains. The growth of a completely modulation-free crystal was not successful in our experiments, which would require the supperession of selective evaporation of Pb in the growth process.

The occurrence of the two-phase region with a miscibility gap must be related to the stability of the structural modulation as a function of Pb content, because the fundamental crystal structure is the same for the two phases. It is known that the Pb substitution makes the modulation period longer and, at the same time, the amplitude of the atomic shifts from ideal positions smaller (30). The existence of the gap implies that weak modulations with λ's longer than a critical value become unstable at low temperature. Such a structural instability can give rise to a driving force for the phase separation. The fact that the stable (010) interface coincides with the plane front of the modulation wave is nothing but substantial evidence of an intimate relation between the two-phase microstructure and the stability of the modulated structure.

Growth Mechanism

The lamellar microstructures found in the present study reminds us of eutectics and eutectoids cooled unidirectionally (31). They usually form either alternating lamellar plates or rods embedded in a matrix. Many examples are known

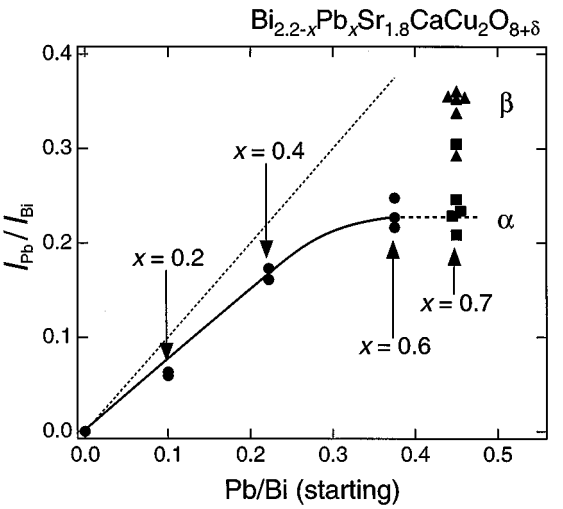

FIG. 15. The intensity ratio of the Lβ_1 + Lβ_2 peaks of Bi and Pb, I_{Pb}/I_{Bi}, plotted as a function of the starting molar ratio of Pb/Bi. The data for $x = 0.2$, 0.4, and 0.6 (circles) were obtained by using a large probe size, while those for $x = 0.7$ by using a 3 nmϕ probe focused on modulated (squares) and modulation-free domains (triangles). The broken line assumes no loss in Pb content during the crystal growth.

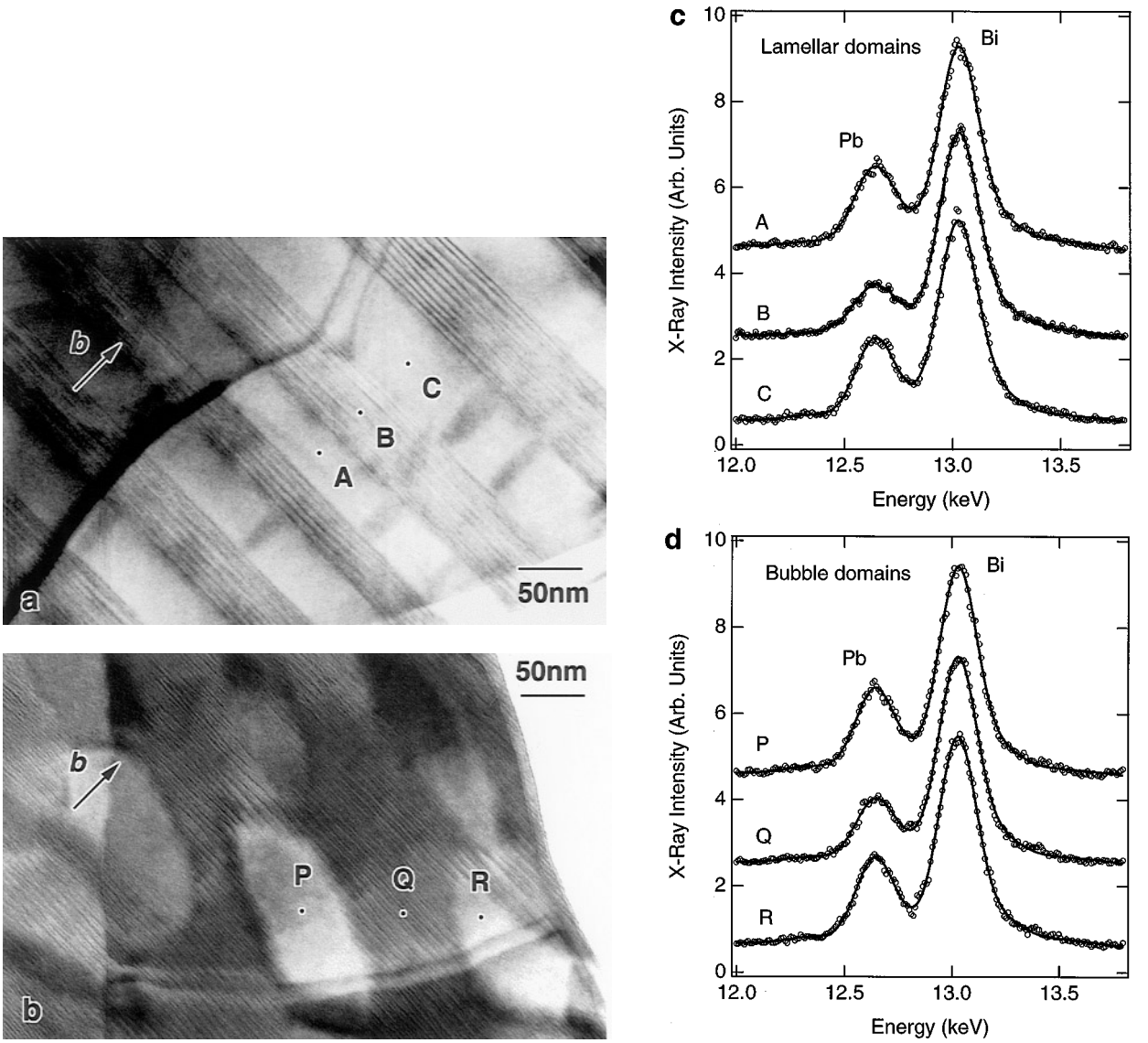

FIG. 16. Microanalysis using a nanometer probe in an analytical electron microscope. Two fragments with (a) lamellar and (b) bubble structures were examined. The position and the approximate size of the probe are shown in each image. The EDX spectra from these points are presented in (c) and (d).

for metallic systems, while recently a large number of oxide–oxide eutectics have also been studied (32, 33). As for cupric oxides, Revcolevschi *et al.* prepared on aligned eutectic structure made of $La_{2-x}Sr_xCuO_4$ and Cu_2O by a FZ technique (34).

The lamellar morphology observed in our study is quite similar to those found in Pb–Sn, $NiO–ZrO_2$, and $Fe(C)–Fe_3C$ (31). Here, the growth mechanism of the present crystals will be considered analogically. As depicted in Fig. 18, the crystal growth using a FZ technique is generally conducted by establishing a floating melt zone between a polycrystalline feed rod (top) and a seed (bottom) and moving both these rods downward slowly. There is a steep temperature gradient on either side of the melt. If the phase diagram is a eutectic type or eutectoid type such as illustrated in Fig. 18, two crystals with different compositions grow from the melt or from the solid solution (ss) stabilized at higher temperature. A composite crystal generally grows with a plane front perpendicular to the growth direction. In the present case, Pb atoms must have been supplied preferentially to the β plates from the melt or from the ss. As the α phase grows, it rejects Pb atoms into the liquid or the ss, and the growing β phase receives the excess Pb atoms. When this growth proceeds in an equilibrium state, alternating plate-like crystals with their interface perpendicular to the growth-front plane are obtained. Since the crystal grows

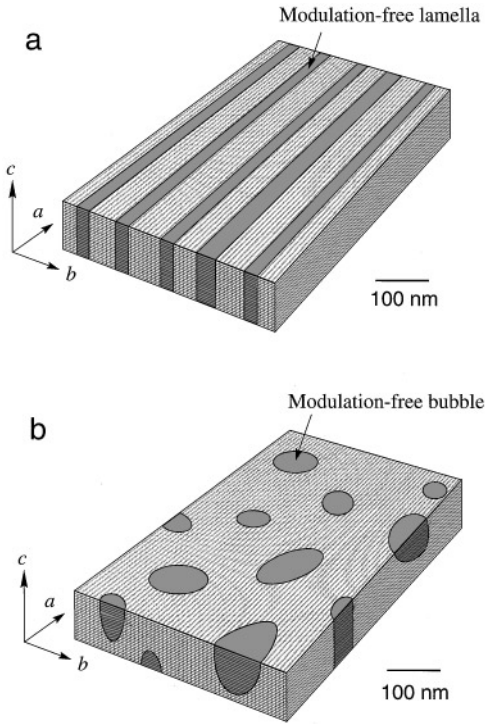

FIG. 17. Schematic representation of the (a) lamella-type and (b) the bubble-type two-phase microstructures found by HREM in heavily Pb-substituted Bi-2212 single crystals.

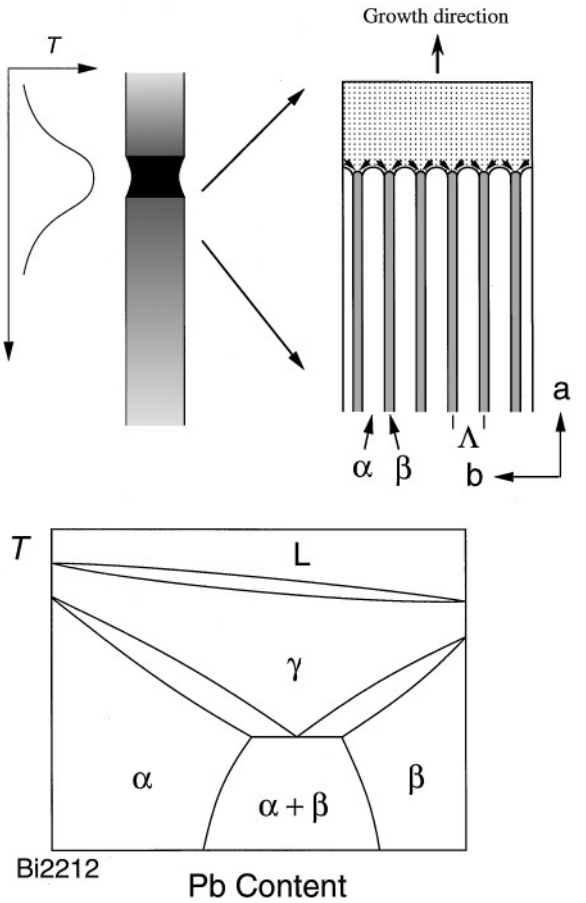

FIG. 18. Schematic representation of the growth mechanism of the lamellar structures and a tentative phase diagram of eutectoid type for the Pb-substituted Bi-2212 system. See text for detail.

along the crystallographic *a* axis, the interface with a low Miller index should be perpendicular to the *b* or *c* axis. The actual choice of the *b* axis must be related to the stability of the modulated structure measured as a function of Pb content as discussed above.

In general, the eutectic type growth occurs only at the eutectic composition. However, we found in the present system that the volume fractions of the two phases varied rather systematically with the average Pb composition, which implied that the growth took place in a wider composition range. This kind of discrepancy has been explained by taking into account constitutional supercooling associated with large temperature gradients in the floating zone method (34).

The lamellar spacing Λ is considered to be determined by the lateral diffusion. The relationship between Λ and the solidification rate R in the eutectic growth has been established both theoretically and experimentally and is of the form $\Lambda^2 \propto 1/R$ (31). Usually, $R \sim 1$–10 cm/h and Λ is a few micrometers in metallic and oxide eutectics. Applying this relation to the present case, Λ should be much larger than experimentally found because R is smaller by two orders of magnitude (~ 1 mm/h). This discrepancy suggests that the present microstructure has been derived from the solid solution (phase γ) rather than directly from the melt, namely, by an eutectoid decomposition, because a diffusion must be much slower in a solid than in a liquid. In fact, a typical lamellar spacing found in the Fe–C eutectoid system is of the same order. Moreover, the experimental result that showed the disappearance of the two-phase structures after annealing at 816°C is evidently consistent with this scenario. It is plausible that, as temperature decreases, fluctuation in Pb concentration occurs in the solid solution and finally results in a phase separation because of the instability of the long modulation at low temperature.

The appearance of irregular lamellas or bubble-shaped β domains for $x \geq 0.7$ suggests that the interface energy is rather small. In usual eutectics the rod morphology appears when the volume fraction of one phase is sufficiently small, approximately 0.2–0.3 (31). In the present crystals, in contrast, round-shaped domains were often found near even fraction. Since the fundamental crystal structure is the same for the α and β phases, the interface energy must be much smaller than in other systems consisting of two crystals with different crystal structures, and the dependence of the interface energy on crystallographic direction must be also small. Then, interfaces inclined from a particular lattice plane with

a low Miller index (e.g., (010)) or round interfaces can be stabilized.

Remarks on Flux Pinning

The improvement in J_c and the upward shift of the IL in the present heavily Pb-doped Bi-2212 single crystals must be due to an automatic, unintended generation of efficient pinning centers. The specific two-phase microstructures must be related to it. The interface always crosses the CuO_2 planes. The situation might be similar for YBa_2 $Cu_3O_{7-\delta}$ with twin boundaries (35). However, the improvement in J_c should be more significant in Bi-2212 because of its inherent strong anisotropy. Another point important to note is that T_c depends upon Pb content; T_c, when optimized, first increases, reaches a maximum of 93 K at $y = 0.2$ or 95 K at $y = 0.4$, and then decreases down to 90 K at $y = 0.6$ (10). Then, the present two phases with different Pb contents could have slightly different T_c's. Thus, the present microscopic two-phase structures must suppress the thermal fluctuation of pancake vortices more efficiently than randomly distributed point defects. A more detailed study to elucidate the role of the microstructures on flux pinning will be reported elsewhere.

CONCLUSIONS

The evolutions of the magnetic properties and the microstructures with Pb substitution in Bi-2212 are studied. A dramatic increase in J_c and a significant upward shift of the IL in the H-T diagram are revealed and principally attributed to the unique two-phase microstructures found by HREM. The presence of the miscibility gap in the Bi-2212–(Bi, Pb)-2212 pseudobinary phase diagram is suggested, in which the alternating lamellar structures consisting of the Pb-poor and modulated α phase and the Pb-rich and modulation-free β phase grow as temperature is decreased below the eutectoid temperature.

ACKNOWLEDGMENTS

We thank K. Yamaguchi and K. Sato (Sumitomo Electric Industries, Ltd.) for help with the EDX measurements in an analytical electron microscope, and Y. Kusano (Kurashiki University of Science and the Arts), T. Shimizu, and J. Takada (Okayama University) for preparation of polycrystalline samples. Discussions with K. Kishio and J. Shimoyama (University of Tokyo) are acknowledged. This work was supported, in part, by CREST (Core Research for Evolutional Science and Technology) of Japan Science and Technology Corporation.

REFERENCES

1. G. Blatter, M. V. Feigel'man, V. B. Geshkenbein, A. I. Larkin, and V. M. Vinokur, *Rev. Mod. Phys.* **66,** 1125 (1994).
2. L. Civale, A. D. Marwick, T. K. Worthington, M. A. Kirk, J. R. Thompson, L. Krusin-Elbaum, Y. R. Sun, J. R. Clem, and F. Holtzberg, *Phys. Rev. Lett.* **67,** 648 (1991).
3. M. Konczykowski, F. Rullier-Albenque, E. R. Yacoby, A. Shaulov, Y. Yeshurun, and P. Lejay, *Phys. Rev. B* **44,** 7167 (1991).
4. J. R. Thompson, Y. R. Sun, H. R. Kerchner, D. K. Christen, B. C. Sales, B. C. Chakoumakos, A. D. Marwick, L. Civale, and J. O. Thompson, *Appl. Phys. Lett.* **60,** 2306 (1992).
5. W. Gerhauser, G. Ries, H. W. Neumuller, W. Schmidt, O. Eibl, G. Saemann-Ischenko, and S. Klaumunzer, *Phys. Rev. Lett.* **68,** 879 (1992).
6. H. Kumakura, H. Kitaguchi, K. Togano, H. Maeda, J. Shimoyama, S. Okayasu, and Y. Kazumata, *J. Appl. Phys.* **74,** 451 (1993).
7. V. Hardy, C. Simon, J. Provost, and D. Groult, *Physica C* **205,** 371 (1993).
8. A. K. Pradhan, S. B. Roy, P. Chaddah, D. Kanjilal, C. Chen, and B. M. Wanklyn, *Phys. Rev. B* **53,** 2269 (1996).
9. M. Takano, J. Takada, K. Oda, H. Kitaguchi, Y. Miura, Y. Ikeda, Y. Tomii, and H. Mazaki, *Jpn. J. Appl. Phys.* **27,** L1041 (1988).
10. N. Fukushima, H. Niu, S. Nakamura, S. Takeno, M. Hayashi, and K. Ando, *Physica C* **159,** 777 (1989).
11. Y. Ikeda, Z. Hiroi, H. Ito, S. Shimomura, M. Takano, and Y. Bando, *Physica C* **165,** 189 (1989).
12. P. Majewski, S. Kaesche, H.-L. Su, and F. Alginger, *Physica C* **221,** 295 (1994).
13. H. Ito, Y. Ikeda, Z. Hiroi, M. Takano, and Y. Bando, *J. Jpn. Soc. Powder Powder Metall.* **38,** 171 (1991).
14. M. Schlichenmaier and S. Kemmler-Sack, *Physica C* **198,** 175 (1992).
15. S. Patil, P. L. Paulose, C. Quitmann, and G. Güntherodt, *J. Magn. Magn. Mater.* **104**–**107,** 521 (1992).
16. T. Mochiku, *in* "Bismuth-Based High-Temperature Superconductors," p. 227. Dekker, New York, 1996.
17. P. Fournier, A. Kapitulnik, and A. F. Marshall, *Physica C* **257,** 291 (1996).
18. Y. L. Wang, X. L. Wu, C.-C. Chen, and C. M. Lieber, *Proc. Natl. Acad. Sci. USA* **87**, 7058 (1990).
19. W. D. Wu, A. Keren, L. P. Le, B. J. Sternlieb, G. M. Luke, and Y. J. Uemura, *Phys. Rev. B* **47,** 8172 (1993).
20. I. Chong, Z. Hiroi, M. Izumi, J. Shimoyama, Y. Nakayama, K. Kishio, T. Terashima, Y. Bando, and M. Takano, *Science* **276,** 770 (1997).
21. J. Shimoyama, Y. Nakayama, K. Kitazawa, K. Kishio, Z. Hiroi, I. Chong, and M. Takano, *Physica C* **281,** 69 (1997).
22. C. P. Bean, *Rev. Mod. Phys.* **36,** 31 (1964).
23. Y. Matsui, H. Maeda, Y. Tanaka, and S. Horiuchi, *Jpn. J. Appl. Phys.* **27,** L361 (1988).
24. E. A. Hewat, M. Dupuy, P. Bordet, J. J. Capponi, C. Chsillout, J. L. Hodeau, and M. Marezio, *Nature* **333,** 53 (1988).
25. S. Ikeda, K. Aota, T. Hatano, and K. Ogawa, *Jpn. J. Appl. Phys.* **27,** L2040 (1988).
26. H. W. Zandbergen, W. A. Groen, F. C. Miljhoff, G. v. Tendeloo, and S. Amelinckx, *Physica C* **156,** 325 (1988).
27. R. Retoux, V. Caignaert, J. Provost, C. Michel, M. Hervieu, and B. Raveau, *J. Solid State Chem.* **79,** 157 (1989).
28. J. L. Tallon, R. G. Buckley, P. W. Gilberd, and M. R. Presland, *Physica C* **158,** 247 (1989).
29. D. J. Werder, C. H. Chen, S. Jin, and R. C. Sherwood, *J. Mater. Res.* **4,** 748 (1989).
30. O. Eibl, *Physica C* **175,** 419 (1991).
31. M. C. Flemings, *in* "Solidification Processing," p. 93. McGraw–Hill, New York, 1974.
32. A. Revcolevschi and G. Dhalenne, *Adv. Mater.* **5,** 657 (1993).
33. A. Revcolevschi and G. Dhalenne, *Nature* **316,** 335 (1985).
34. L. Trouilleux, G. Dhalenne, A. Revcolevschi, and P. Monod, *J. Crystal Growth* **91,** 268 (1988).
35. L. J. Swartzendruber, A. Roitburd, D. L. Kaiser, F. W. Grayle, and L. H. Bennett, *Phys. Rev. Lett.* **64,** 483 (1990).